Supplementary Materials –

Materials and Methods

1.Model equations. Low-frequency microturbulence in weakly collisional magnetised plasmas is appropriately described within the gyrokinetic framework (13). The GYSELA code (16) solves the governing coupled gyrokinetic:

$$B^*_{\|s}\frac{\partial \bar{F}_s}{\partial t} + \boldsymbol{\nabla}\cdot\left(B^*_{\|s}\frac{\mathrm{d}\mathbf{x}_G}{\mathrm{d}t}\bar{F}_s\right) + \frac{\partial}{\partial v_{G\|}}\left(B^*_{\|s}\frac{\mathrm{d}v_{G\|}}{\mathrm{d}t}\bar{F}_s\right) = B^*_{\|s}\,(\mathrm{rhs}) \tag{A-1}$$

$$\mathrm{rhs} = \mathcal{C} + \mathcal{S} + \mathcal{D} - \nu\mathcal{M}^{\mathfrak{mat}}(r,\theta)[\bar{F}_s - \mathbb{G}_{\mathrm{cold}}] - \gamma^K\left[\bar{F}_s - \mathbb{F}_{\text{F-D}}\left(1 + \frac{\langle \bar{F}_s - \mathbb{F}_{\text{F-D}}\rangle}{\langle \mathbb{F}_{\text{F-D}}\rangle}\right)\right] \tag{A-2}$$

and quasi-neutrality:

$$\Delta n_e = \rho + \frac{1}{n_{e_0}}\sum_s Z_s \nabla_\perp\cdot\left(\frac{n_{s_0}}{B\Omega_s}\nabla_\perp\phi\right) \tag{A-3}$$

$$\begin{aligned}\frac{T_e}{e}\Delta n_e = {} & \phi - \lambda\Big[1 - \mathcal{M}^{\mathrm{SOL}}(r)\Big]\langle\,\phi\,\rangle_{\mathrm{FS}} - \Big[\mathcal{M}^{\mathfrak{mat}}(r,\theta) - \mathcal{M}^{\mathrm{wall}}(r)\Big]\phi^{\mathrm{bias}} \\ & - \lambda\Lambda\Big[\mathcal{M}^{\mathrm{SOL}}(r) - \mathcal{M}^{\mathfrak{mat}}(r,\theta)\Big](T_e - T_e^{\mathrm{b.c.}})\end{aligned} \tag{A-4}$$

equations for the guiding-center distribution function $\bar{F}_s$ of ion species s, evolved with no separation between equilibrium and perturbation in five dimensional guiding-centre space $(\mathbf{x}_G, v_{G\|}, \mu)$ and time. In Eq.(A-2), $\langle\cdot\rangle = \int J_{\mathrm{v}}J_{\mathrm{x}}\cdot \mathrm{d}v_\|\mathrm{d}\mu\mathrm{d}\theta\mathrm{d}\varphi$, with J_{v} and J_{x} being the velocity and space Jacobians. The charge density of guiding-centers ρ is computed as:

$$\rho(\mathbf{x},t) = \frac{1}{n_{e_0}}\sum_s Z_s\int \mathrm{d}\mu\mathcal{J}_\mu.\left[\int J_{\mathrm{v}}\,\mathrm{d}v_{G\|}\,(\bar{F}_s(\mathbf{x},\mathbf{v},t) - \bar{F}_{s,\mathrm{eq}}(r,\theta,v_{G\|}))\right] \tag{A-5}$$

with $\mathcal{J}_\mu.$ the gyro-average operator. Notations are those of Ref.(14). The computational domain extends from inner core ($r/a = 0$) to the material boundaries ($r/a = 1.3$). Flux- or gradient-driven dynamics may be considered. For flux-driven evolution, $\gamma^K = 0$ and the distribution function evolves according to volumetric sources $\mathcal{S}$ (31) and penalised heat and momentum sinks $\mathcal{M}^{\mathfrak{mat}}(r,\theta)$, $\mathcal{M}^{\mathrm{SOL}}(r)$ and $\mathcal{M}^{\mathrm{wall}}(r)$ that can mimic from poloidally-uniform boundary conditions (Case-2) to the more complex limiter and wall geometries (Case-1). The latter case allows description of the closed to open field lines transition in the Scrape-Off Layer (SOL). Gradient-driven-like dynamics may also be considered whilst imposing $\mathcal{S} = \mathcal{M}^{\mathfrak{mat}}(r,\theta) = \mathcal{M}^{\mathrm{wall}}(r) = 0$. In Case-3, the target distribution function

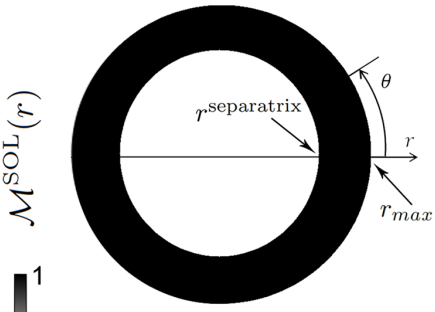

Tokamak volume	Mask
All plasma	$1-\mathcal{M}^{\rm mat}(r,\theta)$
Closed field lines	$1-\mathcal{M}^{\rm SOL}(r)$
Scrape-Off Layer	$\mathcal{M}^{\rm SOL}(r)-\mathcal{M}^{\rm mat}(r,\theta)$
Material boundaries	$\mathcal{M}^{\rm mat}(r,\theta)$
Limiter only	$\mathcal{M}^{\rm mat}(r,\theta)-\mathcal{M}^{\rm wall}(r)$
Wall only	$\mathcal{M}^{\rm wall}(r)$

Fig. A-1. The various masks used for penalisation in the gyrokinetic–Poisson system.

$\mathbb{F}_{\text{F-D}}$ is chosen as the statistical distribution at equilibrium from flux-driven Case-2 and the relaxation rate $\gamma^K = 5.43\,10^{-5} \sim \gamma_{lin}/10$ is an order of magnitude smaller than the local linear turbulence growth rate γ_{lin} at $r/a = 0.7$. Imposing $\mathcal{M}^{\rm SOL}(r)$ as in Case-2 or cancelling this mask does not alter the dynamics which is dominated by the BGK operator [last term of Eq.(A-2)], specifically described in Ref.(32) and built such as to prevent overdamping zonal modes (33).

Penalisation (34) modifies the equations through introduction of a series of masks $\mathcal{M}^{\rm mat}(r,\theta)$, $\mathcal{M}^{\rm SOL}(r)$ and $\mathcal{M}^{\rm wall}(r)$, combinations of hyperbolic tangents, adjustable in location, shape (for $\mathcal{M}^{\rm mat}(r,\theta)$) and stiffness. They are illustrated in Fig.A-1. Electrons have a Boltzmann response modified by penalisation such that the electric potential ϕ in the quasi-neutrality equation is relaxed towards its expected presheath condition $\Lambda T_e/e$ in the SOL. Additionally, ϕ may be biased to $\phi^{\rm bias}$ in the limiter ($\phi^{\rm bias} = 0$ in the current study) and is freely evolving elsewhere. $T_e^{\rm b.c.}$ is the cold electron temperature within limiter and wall, chosen as the minimum T_e value within the computational domain, $\Lambda = \log(\sqrt{m_i/m_e})$ and coefficient λ (set to unity in the present study) may be used to alter the inertia of the zonal potential. In the gyrokinetic equation, infinite penalisation (35) relaxes

$\bar{F}_s$ to a target cold Maxwellian distribution function $\mathbb{G}_{\rm cold} = n_{\rm w}(2\pi T_{\rm w})^{-3/2}\exp[-(v_{G\|}^2 + \mu B)/2T_{\rm w}]$, characterised by low wall thermal energy $T_{\rm w}$ and target density $n_{\rm w}$. The former is constrained by velocity-space resolution; we typically choose it an order of magnitude lower that temperature at mid radius whilst the target density $n_{\rm w}$ is chosen so as to ensure particle conservation.

2.Physical parameters and robustness. The reference Tore Supra shot 45511 had 2MW of Ion Cyclotron Resonance Heating on top of 1MW of Ohmic heating injected in a deuterium plasma of normalised size $\rho_\star = \rho_i/a = 1/500$ at mid radius and aspect ratio $a/R_0 = 1/3.3$, a and R_0 being respectively the minor and major radius. The plasma current is $I_p = 0.8$MA, the magnetic field on axis is $B_0 = 2.8$T and the density and temperature at mid-radius respectively read: $n = 4\,10^{19}\mathrm{m}^{-3}$ and $T = 0.8$keV. In GYSELA, a 3MW volumetric heat source comparable in shape to that in the experiment is injected in the central 40% of a deuterium torus of same aspect ratio. Initial density, electron and ion temperature profiles are the same as in the experiment up to the separatrix. In the core $T_e/T_i > 1$ whilst this ratio reverses in the edge and SOL. To slightly offset the numerical cost of the computations, run on Tier-0 Joliot-Curie at GENCI@CEA and MareNostrum at Barcelona Supercomputing Center, we assume a reduced magnetic field on axis: $B_0 = 1.7$T, which amounts to computing a plasma column of slightly smaller size $\rho_\star = 1/300$ on a 1/4 wedge torus with $(r, \theta, \varphi, v_\|, \mu) = (512, 1024, 64, 128, 64)$ grid.

Extensive tests have been performed to assess the robustness of the reported main results: observed gradient anisotropy and magnitudes in the limited configuration are robust whilst varying distribution function initialisation (local or canonical Maxwellians), presheath values in the SOL through Λ scans (from 0 to 5, its nominal value for Deuterium being $\Lambda \sim 4.1$), target penalised temperature $T_{\rm w}$ in the limiter and wall, limiter shape (large and flat, narrow, rounded) and poloidal location (bottom, top). Further scans have also been performed in a flux-driven poloidally symmetric setting akin to Case-2, varying the T_e/T_i ratio, changing the safety factor q and magnetic shear s and altering the experimental density gradient. The latter two are illustrated in Fig.A-2. Of course, details of edge transport vary with the various parameters scanned. Precise discussion of sensitivity is not within the scope of the current manuscript; the bottomline conclusion is that the reported dynamics of Case-1 (modified outer edge linear stability, nonlinear destabilisation and ensuing transport barrier onset) requires the combined possibility for plasma-boundary interplay and turbulence spreading. Absence

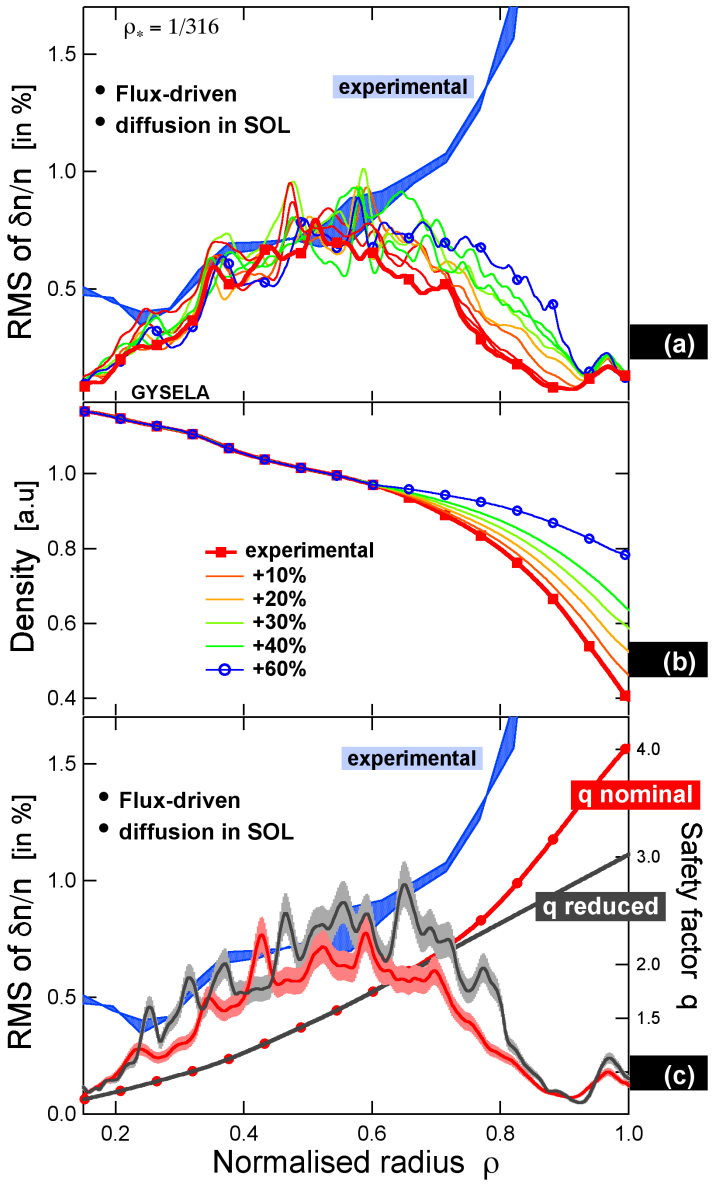

Fig. A-2. Series of flux-driven computations at $\rho_\star = 1/316$, akin to Case-2 but for the outer boundary conditions. In lieu of the penalised poloidally symmetric SOL of Case-2, an outer diffusive buffer region between $1 \leq r/a \leq 1.3$ surrounds the confined plasmas through application of the diffusion operator $\mathcal{D}$ in Eq.(A-2), detailed as Eq.(50) in (14). The goal is twofold: assess sensitivity (beyond experimental uncertainties) of edge transport dynamics to variations or uncertainties in input profiles and evaluate incidence of surrounding artificial diffusion for edge transport. Density gradients have a stabilising effect on the dominant Ion temperature Gradient (ITG) instability. Subplots (a) and (b) display incremental relaxation of density gradients past $r/a \geq 0.6$ and their incidence on fluctuation levels. Similarly, lower magnetic shear and safety factor values past $r/a \geq 0.6$ modestly increase fluctuations there. In all cases, edge fluctuation levels are lower than in comparable Case-2. In the absence of outer edge turbulent activity, core to edge spreading appears subdominant. Technically, the choice of an outer diffusive boundary region, though efficient numerically is thus not innocuous (and probably quite poor) on physical grounds.

of one or both prevents as in Cases-2 and 3 transport barrier onset and leads to transport shortfalls in NMsL of varying severity.

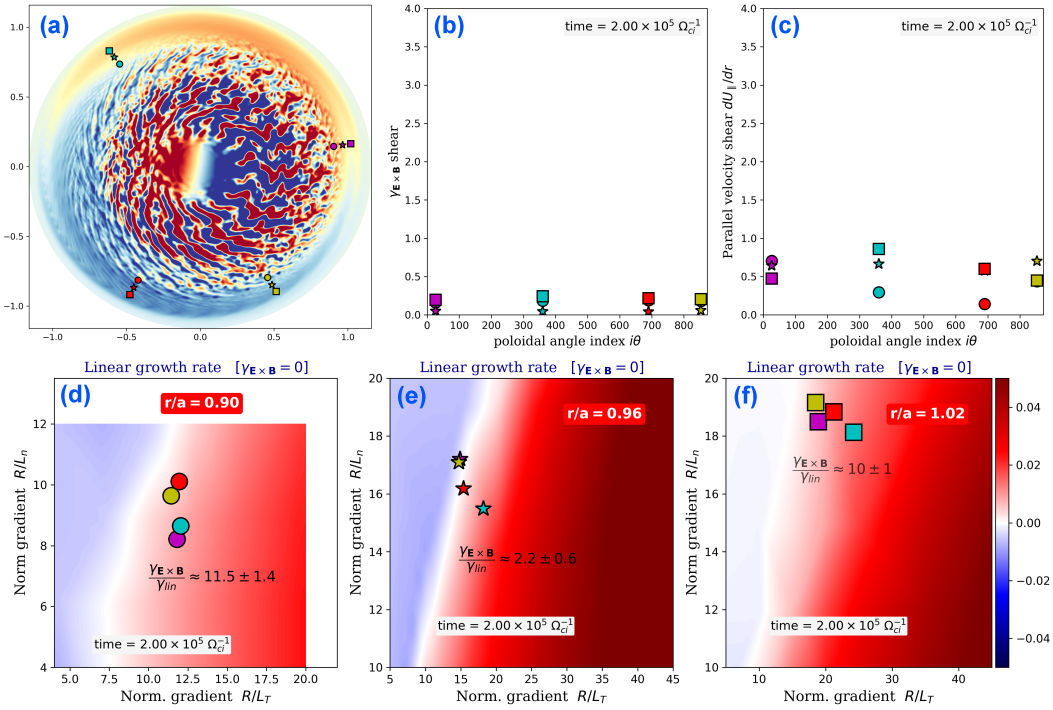

Fig. A-3. Data from flux-driven poloidally-symmetric Case-2, at equilibrium ($t\Omega_{ci} = 200,000$). (a) Poloidal cross-section snapshot of the fluctuating electric potential. Specific locations are marked, combination of three radial locations: $\{r_1, r_2, r_3\}/a = \{0.90$ (circles)$, 0.96$ (stars)$, 1.02$ (squares)$\}$ and four poloidal locations $\theta_k = \{9°$ (magenta)$, 126°$ (cyan)$, -118°$ (red)$, -61°$ (yellow)$\}$. Properties at these locations are shown in subplots (b): $\mathbf{E} \times \mathbf{B}$ shear, (c): parallel velocity shear and (d) through (f): maximul linear instability growth rate at vanishing $\mathbf{E} \times \mathbf{B}$ shear, keeping the same symbol–color combination.

3.Linear stability analysis of the poloidally-symmetric and limited GYSELA profiles is performed using the initial value framework of the Gyrokinetic Workshop (GKW) code (17), based on the gradient-driven and local (flux-tube) approximations. Unless stated otherwise (see Strategy III below) Boltzmann electrons have been assumed, as in GYSELA. Growth rates for the most unstable poloidal wavenumbers $k_\theta \rho_i = 0.6$ in the poloidally-symmetric (Fig.A-3) and limited (Fig.A-4) configurations are estimated by the following procedure.

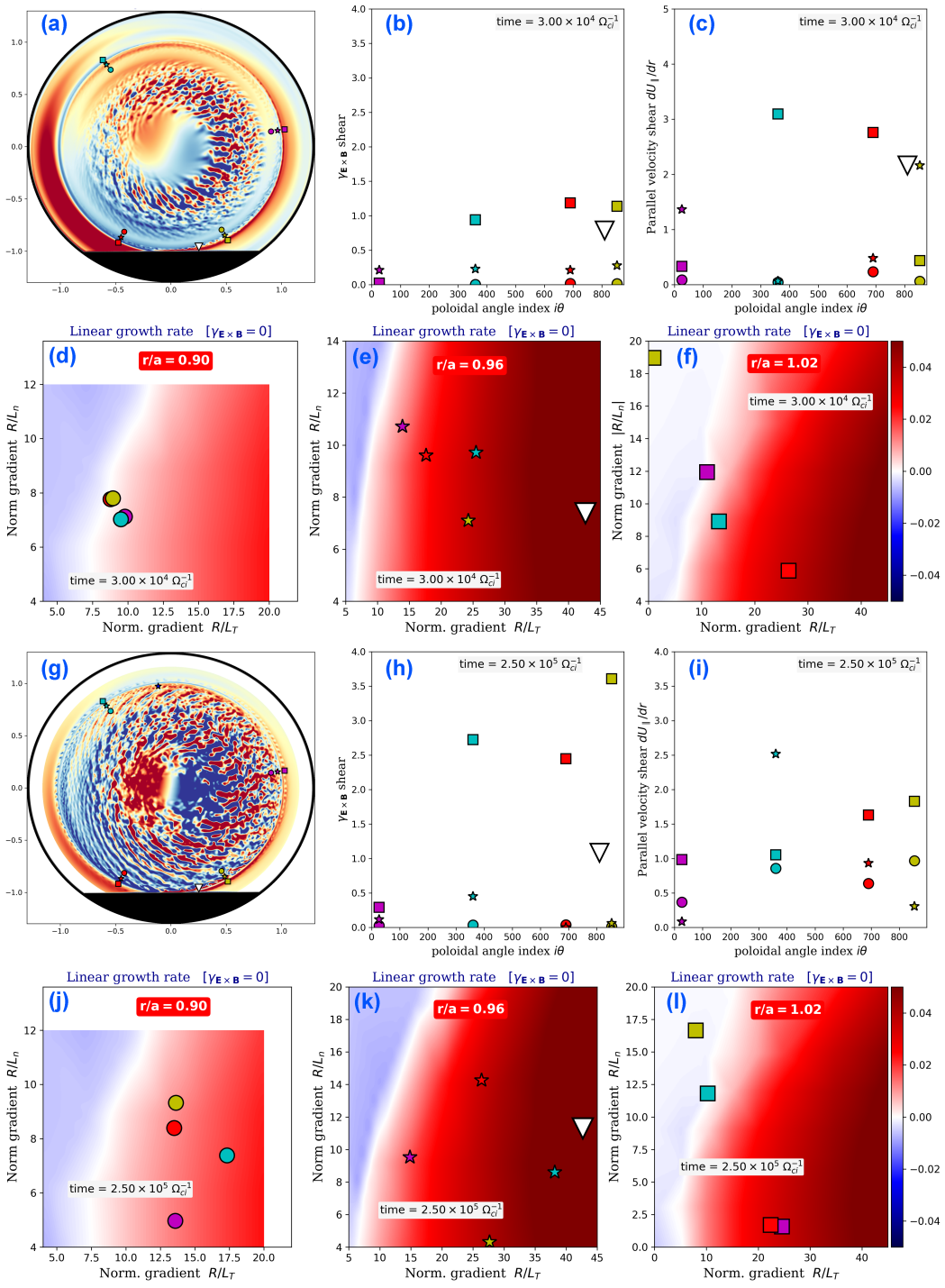

Fig. A-4. Same layout as in Fig.A-3. Data is from flux-driven Case-1 with limiter at two different times: subplots (a) through (f) are early in the nonlinear development of turbulence ($t\Omega_{ci} = 30,000$); subplots (g) through (l) at thermal equilibrium ($t\Omega_{ci} = 250,000$). An additional location near the limiter at ($r/a = 0.96, \theta = -75°$), marked by the large white triangle is shown and corresponds to the region of maximum linear instability growth.

(i) at a given radial location r_0, compute the set $\Sigma_{r_0} = \{q, s, \nu_\star, T_i/T_e, U', \gamma_E, R/L_T, R/L_n\}$ of local values of the GYSELA plasma parameters, q being the safety factor, $s = (r/q)dq/dr$ the magnetic shear, $\nu_\star$ is the collisionality, U' the parallel flow shear, γ_E denotes the $\mathbf{E} \times \mathbf{B}$ shear, R the tokamak major radius and $L_X^{-1} = -d(LogX)/dr$ with $X = \{T, n\}$ the local logarithmic gradients of respectively ion temperature and density;

(ii) within GKW, the local approximation requires mean gradients to be constant over the computational domain, the numerical representation of a flux tube. Coarse-graining of the flux-driven GYSELA values is thus performed over a typical radial turbulence length scale $\Delta r = 10\rho_i$ and in time over the observed linear growth $\Delta t\, \Omega_{ci} = 25\, 10^3$ of turbulent fluctuations. Furthermore, as the computational domain of GKW winds around the torus parsing both poloidal and toroidal angles, the background state is assumed to be uniform. This implies poloidal homogeneity along the flux tube and requires further averaging the GYSELA values on a flux-surface (θ, φ): $\langle\langle\langle\langle\Sigma_{r_0}\rangle_{\Delta t}\rangle_{\Delta r}\rangle_\theta\rangle_\varphi$, where $\langle\cdot\rangle_\zeta$ denotes the average over ζ. Physically, it amounts to estimating the instability drive as if located at its ballooning angle, effectively maximising it;

(iii) for a chosen radial location r_j, knowing $\langle\langle\langle\langle\Sigma_{r_j}\rangle_{\Delta t}\rangle_{\Delta r}\rangle_\theta\rangle_\varphi$ allows to compute with GKW 2-dimensional maps of instability growth rates γ_{lin} as a function of the logarithmic gradients [subplots Fig.A-3-(d) to (f) and Fig.A-4-(d) to (f) and (j) to (l)], each map tailored to the precise background local values in GYSELA for T_i/T_e, etc. Importantly, these maps are estimated at vanishing $\mathbf{E} \times \mathbf{B}$ shear;

(iv) we now estimate local values of the GYSELA local growth rates $\gamma_{\rm lin}$ at 13 different radial-poloidal (r_j, θ_k) locations (shown in Fig.1 as well), combination of three radial locations near the separatrix: $\{r_1, r_2, r_3\}/a = \{0.90\ \text{(circles)}, 0.96\ \text{(stars)}, 1.02\ \text{(squares)}\}$ and five poloidal locations $\theta_k = \{9°, 126°, -118°, -75°, -61°\}$, spanning the full poloidal cross-section;

(v) in order to assess actual stability, one can estimate an effective linear growth rate correcting for the $\mathbf{E} \times \mathbf{B}$ shear: $\gamma^{\rm eff} = \gamma_{\rm lin} - \gamma_E$ [strategy I] or run GKW nonlinearly, including γ_E from GYSELA [strategy II]. This latter strategy is significantly more demanding numerically and only a few cases have been investigated. Furthermore, 2 additional runs with GKW have been performed

at $(r/a = 0.84, \theta = 9°)$ and $(r/a = 0.96, \theta = 9°)$ with a fully kinetic electron response to assess the impact of the Boltzmann electron approximation [strategy III].

For all Cases, the dominant instabilities inside $r/a \leq 0.84$ are found to be of interchange character. With a Boltzmann electron response, the ion temperature gradient (ITG) is dominant. With a kinetic electron response the instability inside $r/a \leq 0.84$ is a combination of ITG and Trapped electron modes (TEM).

- In poloidally-symmetric Cases-2 and 3, GKW finds the edge to be marginally stable at vanishing $\mathbf{E} \times \mathbf{B}$ shear: $\gamma_{\text{lin}} \approx 0$ [Fig.A-3-(d) to (f)]. When including $\mathbf{E} \times \mathbf{B}$ shear, strategy I predicts the edge to be nonlinearly unconditionally stable past $r/a \geq 0.9$, with $\gamma^{\text{eff}} < 0$ for all radial–poloidal combinations considered. Strategies II and III confirm that location $(r/a = 0.96, \theta = 9°)$ is indeed stable. Contributions of perpendicular and parallel shear flow (parallel velocity gradient, PVG) instability (36) are weak [Fig.A-3-(c)] and insufficient to destabilise NMsL.

- In Case-1 with limiter the situation dramatically changes: destabilisation of the outer edge starts about the limiter, just inside the separatrix. Fig.A-4-(e) shows estimated ITG growth rates at $r/a = 0.96$ that are larger than in Cases-2 and 3 whilst all locations at $r/a = 0.9$ remain stable [Fig.A-4-(a) and (d)]. Effective growth rates are large in the vicinity of the limiter at locations $\theta = -75°$ and $-61°$. Instability growth is also predicted at the plasma top $\theta = 126°$. Interestingly, as the limiter remains a cold sink throughout nonlinear regime, the near-limiter drive endures [Fig.A-4-(k)] and as turbulence spreads, formerly stable regions are destabilised [Fig.A-4-(g) and (j)]. Both $\mathbf{E} \times \mathbf{B}$ shear [Figs.A-4-(b) and (h)] and parallel velocity gradient [Figs.A-4-(c) and (i)] are significantly increased with respect to poloidally-symmetric Cases-2 and 3. The significant velocity shear near the separatrix is found to contribute a modest albeit positive fraction of the global instability with $\gamma^{\text{PVG}} \equiv |M_{\parallel} L_{v_{\parallel}}^{-1}| - |L_n^{-1}| \approx 0$, when averaged on a flux surface. Here $M_{\parallel}$ is the parallel Mach number. Local values however of parallel velocity shear about the limiter may locally reach up 3 to 5 times the mean with $\gamma^{\text{PVG}} \gtrsim 0$, which does not rule out the possibility for localised yet significant free energy sources from parallel shear flow instability.

It is important to note that even though this procedure provides information on the nature of

instabilities at play, two major and oft-made approximations in local approaches should be relaxed to accurately interpret flux-driven dynamics near the separatrix. Indeed, the local $\mathbf{E} \times \mathbf{B}$ shearing rates obtained from limited GYSELA with respect to poloidally-symmetric cases [respectively comparing Figs.A-4-(b) and (h) to Fig.A-3-(b)] are large enough to significantly decrease linear growth, as currently estimated through GKW. Strategy I balancing maximum growth with $\mathbf{E} \times \mathbf{B}$ shear only provides partial insight into the nature of active instabilities. Secondly, postulating poloidal (parallel) homogeneity as flux tubes wind around the torus is reasonably accurate in the core but clearly less justifiable to describe the near-separatrix in flux-driven limited configurations. Much of the nonlinear destabilisation of linearly stable edge is consequence of the onset of such poloidal inhomogeneities. Furthermore, additional stabilisation mechanisms are possible, such as profile coupling or poloidal shift of the envelope mode. This linear analysis thus likely provides an upper-bound estimate of the actual flux-driven instability growth. It has the merits however to confirm that the edge under poloidally-symmetric boundary conditions is linearly stable and that it gets destabilised locally in the vicinity of the cold sink, emphasising the central role of turbulence spreading in understanding global equilibration of the turbulence dynamics.

4.Causal inference. Causality detection in information theory is actively debated (25). The "Transfer Entropy" (TE) method is a simple nonlinear extension of the Granger causality (28), introduced by Schreiber (26) and investigated in magnetised plasmas by Van Milligen et al. (27). The idea behind TE is simple: let's consider a time series (x_i) of realisations of observable X, with $0 \leq i \leq n$. If one can better predict its next realisation x_{n+1} using additional data from another time series (y_j) of observable Y with $0 \leq j \leq n$, then "Y transfers information (i.e. causes) X", or more accurately as "Y forecasts X", which constitutes the definition of causality here. This idea is quantified measuring deviation of transition probabilities from independence, i.e. from a stationary Markov process. In its simplest expression, if processes X and Y are independent, then the following generalised Markov property holds for all $0 \leq k \leq n$: $p(x_{n+1}|x_{n-k}, y_{n-k}) = p(x_{n+1}|x_{n-k})$. The standard notation for conditional probabilities is used here: $p(a|b)$ is the probability of a knowing b. If now processes X and Y are not independent, the ratio of these two transition probabilities provides a measure of how much information they may share. In other words, how much knowing values within Y in addition to past values in X may help to better evaluate next-step x_{n+1}. This idea leads to the following definition of

the Transfer Entropy (TE) from process Y to process X:

$$TE_{Y\to X}(k) = \sum p(x_{n+1}, x_{n-k}, y_{n-k}) \log\left(\frac{p(x_{n+1}|x_{n-k}, y_{n-k})}{p(x_{n+1}|x_{n-k})}\right) \tag{A-6}$$

where k is thus a time lag and represents the k-past of times series X and Y. The summation process is detailed below, in Eq.(A-8). TE can equivalently be recast as a conditional mutual information and represents the additional amount of information that must be added to adequately represent the studied process $p(x_{n+1}|x_{n-k}, y_{n-k})$ with respect to its reference Markov process $p(x_{n+1}|x_{n-k})$. In the absence of information flow from Y to X, the logarithm vanishes as state Y has no influence on the transition probabilities of X. It also follows that TE is directional, i.e. $TE_{Y\to X} \neq TE_{X\to Y}$, effectively allowing to infer causality between processes X and Y. TE displays interesting properties: it is independent of the relative magnitudes of signals X and Y; it may apply to either linear and nonlinear regimes; it is easy to evaluate directly in real space rather than in Fourier space and is typically less demanding in terms of statistics than bispectral techniques. Practically, TE is evaluated expressing the conditional probabilities as joint probabilities $p(x_{n+1}|x_{n-k}, y_{n-k}) = p(x_{n+1}, x_{n-k}, y_{n-k})/p(x_{n-k}, y_{n-k})$ and computing the 4 multidimensional probability density functions (pdfs):

$$TE_{Y\to X,\alpha}(k) = \sum p^{\alpha}(x_{n+1}, x_{n-k}, y_{n-k}) \log^{\alpha}\left(\frac{p(x_{n+1}, x_{n-k}, y_{n-k})\, p(x_{n-k})}{p(x_{n+1}, x_{n-k})\, p(x_{n-k}, y_{n-k})}\right) \tag{A-7}$$

as a function of time delay k and normalised such that $0 \leq TE \leq 1$. The 4 pdfs in Eq.(A-7) result from a binning process of times series X and Y, such that Eq.(A-7) is estimated in practice as:

$$TE_{Y\to X,\alpha}(k) = \sum_{i=1}^{\beta}\sum_{j=1}^{\beta}\sum_{l=1}^{\beta} \left[p^{3d}(i,j,l)\right]^{\alpha} \log^{\alpha}\left(\frac{p^{3d}(i,j,l)\, p^{1d}(j)}{p^{2d}_{xx}(i,j)\, p^{2d}_{xy}(j,l)}\right) \tag{A-8}$$

where p^{3d}, p^{2d}_{xx}, p^{2d}_{xy} and p^{1d} are the discretised versions of respectively $p(x_{n+1}, x_{n-k}, y_{n-k})$, $p(x_{n+1}, x_{n-k})$, $p(x_{n-k}, y_{n-k})$ and $p(x_{n-k})$. In order to have sufficient statistics, a bin size $\beta = 2$ or $\beta = 3$ is typically chosen, depending on the available length of the time series (the longer the times series, the larger β can be). We introduced here the additional exponent $\alpha \geq 1$, which effectively represents a nonlinear threshold: low probabilities will be further reduced and higher ones amplified. In a complex setting, information may flow both ways, from Y to X and inversely. It is thus especially useful to define the net transfer entropy $\Delta_{X,Y}(TE)[k] = TE_{Y\to X}[k] - TE_{X\to Y}[k]$, which provides the net flow of information between processes X and Y, at timelag k. In the manuscript, pdfs in Eq.(A-7) are discretised

using $\beta^d = 2^d$ bins, with d the dimensionality of the pdf. The nonlinear threshold exponent α is set to unity and X and Y are discretised at the same rate and enter the TE calculation with zero temporal mean. Further details may be found in (24).

We systematically apply the TE algorithm to actual time series from the flux-driven Case-1 computation with limiter boundary conditions in the last 5% inside the separatrix, where the spontaneous onset of a persistent transport barrier is observed. The following vorticity equation can be inferred from the primitive gyrokinetic equations including $\mathbf{E} \times \mathbf{B}$ drift and finite Larmor radius at leading order:

$$\partial_t \langle \Omega_r \rangle + \frac{1}{r}\partial_r r \left[\langle v_{Er}\Omega_r \rangle + \langle v_{\star r}\Omega_r \rangle - \left\langle v_{\star\theta}\frac{1}{r}\partial_\theta E_r \right\rangle \right] = r.h.s \tag{A-9}$$

$$r.h.s \approx -\partial_t \langle \Omega_\theta \rangle - \frac{1}{r}\partial_\theta \langle (v_{E\theta} + v_{\star\theta})\Omega_\theta \rangle - \partial_r \frac{1}{2r}\partial_\theta \langle v_{E\theta}^2 \rangle + \frac{1}{2r^3}\partial_\theta \partial_r \langle r^2 v_{Er}^2 \rangle - \frac{1}{r}\partial_\theta \left\langle v_{\star r}\frac{1}{r}\partial_\theta v_{E\theta} \right\rangle \tag{A-10}$$

$$\Omega_r = \partial_r \left(r\partial_r \phi \right)/r \qquad \& \qquad \Omega_\theta = \partial_\theta^2 \phi / r^2 \tag{A-11}$$

$$v_{Er} = -\partial_\theta \phi / r \qquad \& \qquad v_{E\theta} = \partial_r \phi = -E_r \tag{A-12}$$

$$v_{\star r} = -\partial_\theta p_\perp / r \qquad \& \qquad v_{\star\theta} = \partial_r p_\perp \tag{A-13}$$

where $\langle \cdot \rangle$ denotes an average over toroidal angle φ. The TE algorithm is applied to many of the possible permutations of quantities in Eq.(A-9) and especially here to the following set:

$$(X, Y) \in \left\{ \langle \Omega_r \rangle, \langle v_{Er}\Omega_r \rangle, \langle v_{\star r}\Omega_r \rangle, -\left\langle v_{\star\theta}\frac{1}{r}\partial_\theta E_r \right\rangle \right\} \tag{A-14}$$